Journal of Applied Electrochemistry **32**: 241–249, 2002.

The voltage of alumina reduction cells prior to the anode effect

H. VOGT[1] and J. THONSTAD[2]
[1]*TFH Berlin – University of Applied Sciences, Laboratory for Reaction Technology, D-13353 Berlin, Germany*
[2]*Department of Materials Technology and Electrochemistry, Norwegian University of Science and Technology, 7491 Trondheim, Norway*

Received 28 August 2001; accepted in revised form 19 February 2002

Key words: aluminium electrolysis, anode effect, fluid dynamics, gas evolution, overvoltage

Abstract

Alteration in cell voltage of industrial cells after each feeding of fresh alumina is initially small and accelerates to become extremely fast immediately prior to the incipience of the anode effect. Estimates of the components of the cell voltage on the basis of a mathematical model particularly taking account of the action of the gaseous phase underneath the anode are compared with experimental data from industrial cells. The fundamental agreement (in spite of inevitable model insufficiencies) supports the view that the anode effect is induced as the actual anodic current density approaches the limiting one.

List of symbols

a	activity (dimensionless)
A	initial electrode surface area facing downwards (m^2)
A^*	area covered by macrobubbles (m^2)
A^{**}	area covered by small bubbles (m^2)
b	Laplace parameter, Equation 23 (m)
c	concentration (mol m^{-3})
C_1	constant, Equation 17 (m^2 $A^{-0.5}$ s^{-1})
d	final equivalent microbubble diameter (m)
D	diffusion coefficient (m^2 s^{-1})
E	equilibrium reaction potential (V)
E_0	standard potential (V)
F	faradaic constant, $F = 96\,487$ A s mol^{-1}
f_A	fraction of the anode area rounded off
f_G	gas evolution efficiency
f_I	fraction of the current passing through the electrode side walls
g	acceleration due to gravity (m s^{-2})
H	height of macrobubbles (m)
H^{**}	height of microbubbles (m)
I	total current (A)
j	actual current density (A m^{-2})
j_0	exchange current density (A m^{-2})
k	mass transfer coefficient (m s^{-1})
K	multiplier, Equation 22
K_1	multiplier in Equation 2
K_2	parameter, Equation 25
L	length of electrode edge crossed by bubbles (m)
M	molar mass (kg mol^{-1})
n	charge number
N	amount of substance (mol)
p	pressure (kg m^{-1} s^{-2})
R	universal gas constant, $R = 8.3143$ kg m^2 s^{-2} mol^{-1} K^{-1}
Sc	Schmidt number, $Sc \equiv \eta_L D_A^{-1} \rho_L^{-1}$
T	temperature (°C, K)
U_Ω	ohmic voltage drop (V)
v	velocity (m s^{-1})
w	alumina mass fraction
Y	interelectrode distance (m)

Greek symbols

α	charge transfer factor
γ	interfacial tension
ε	current efficiency
η	anodic overpotential (V)
η_L	liquid viscosity (kg m^{-1} s^{-1})
ϑ	contact angle
Θ^*	fractional shielding of the electrode surface by large bubbles
Θ^{**}	fractional shielding of the electrode surface by small bubbles
κ	electrical conductivity of melt (A m^{-1} V^{-1})
υ	stoichiometric number
ρ_G	gas density (kg m^{-3})
ρ_L	liquid density (kg m^{-3})

Subscripts

A	oxygen-containing ion
B	dissolved gas
c	critical
lim	limiting
max	maximum
w	electrode
∞	liquid bulk

1. Introduction

It is known that the incipience of the anode effect in aluminium electrolysis is preceded by an initially very slow increase in the cell voltage, which gradually accelerates until the voltage increases extremely rapidly immediately prior to the anode effect. The final increase in the voltage by some volts within a few milliseconds is considered as the incipience of the anode effect. This behaviour has been reported repeatedly [1, 2]. Data obtained in industrial cells have been published by Taylor et al. [3], Thonstad et al. [4] and by Meyer and Earley [5], Figure 1. A corresponding very rapid decrease of current in potentiostatic experiments was observed in aqueous solution [6].

The mechanism inducing the anode effect continues to be a controversial subject, although numerous workers have attempted to elucidate it within the past one and a half centuries after the first description of the effect [1]. New interest has been focused on the anode effect when the environmental problems linked with the emission of the perfluorocarbon gases CF_4 and C_2F_6 prior to, and mainly during, the occurrence of the anode effect were recognized. These are powerful greenhouse gases with extremely long lifetimes. To decide on the controlling mechanism of the anode effect, mathematical models have been found to be suitable tools [8–11]. Their quantitative evaluation gave rise to the conclusion that the anode effect is induced by the combined action of wettability and fluid dynamics of bubble release when the limiting current density is attained in continuous cell operation. The explanation combines findings and conclusions with respect to the effect of wetting [12, 13] and those on gas release with the finding by Thonstad [14] of the impact of the limiting current density. The action of hydrodynamics on the tendency of forming sparks was studied in a very different field, namely in electrochemical machining, by Cougar and coworkers [15].

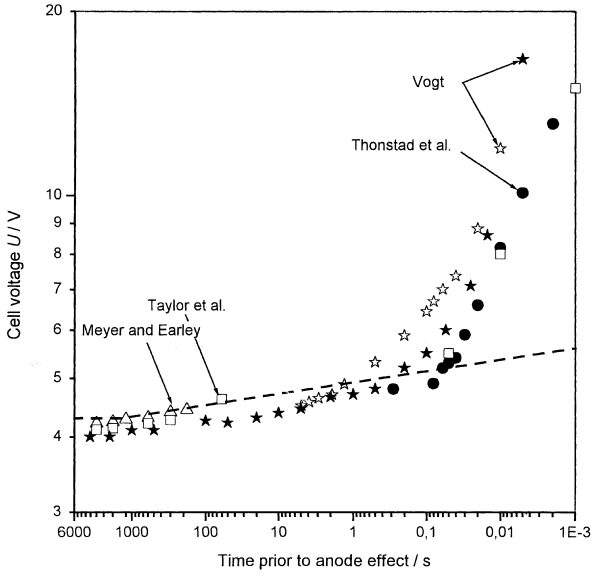

Fig. 1. Cell voltage prior to the onset of anode effect in industrial cells. Key: (□) Taylor et al. [3], (△) Meyer and Earley [5], (●) Thonstad et al. [4], (★, ☆) own measurements. Broken line is calculated.

The object of the present paper is a quantitative analysis of the drastic increase in cell voltage as observed in industrial cells [3, 4] by means of a mathematical model. The steady decrease in alumina concentration in combined action with the resulting deterioration of wettability and in turn the decrease in current passing the anode surface facing downwards will be taken into account to improve the model. A comparison with experimental results obtained on industrial cells is expected to deliver information on the mechanism of the anode effect.

2. Variation of alumina concentration with time

From the depletion of oxygen-containing ions, expressed as that of alumina (subscript A), according to Faraday's law

$$\frac{\mathrm{d}N_\mathrm{A}}{\mathrm{d}t} = -\frac{I\varepsilon_\mathrm{A}}{(n/v_\mathrm{A})F} \tag{1}$$

and with the assumption of uniform alumina bulk concentration $c_{\mathrm{A}\infty}$ in the melt of a total volume being larger than the interelectrode volume YA by a factor K_1, the variation in the alumina concentration follows as

$$\frac{\mathrm{d}c_{\mathrm{A}\infty}}{\mathrm{d}t} = -\frac{I\varepsilon_\mathrm{A}}{(n/v_\mathrm{A})FK_1YA} \tag{2}$$

Although it is known that there are slight concentration gradients in industrial cells, estimates show that mixing is sufficiently rapid to ensure nearly uniform concentration in the melt some time after adding fresh alumina. Substituting the concentration by the mass fraction (or mass content) of alumina w in the liquid bulk,

$$c_{\mathrm{A}\infty} = w\frac{\rho_\mathrm{L}}{M_\mathrm{A}} \tag{3}$$

gives the time prior to the onset of the anode effect provided no further alumina is fed,

$$t_\mathrm{c} - t = \frac{(n/v_\mathrm{A})FK_1Y_{\rho_L}}{(I/A)\varepsilon_\mathrm{A}M_\mathrm{A}}(w - w_\mathrm{c}) \tag{4}$$

where t_c denotes the point of time when reaching the critical alumina content w_c.

3. Bubble coverage

Gas bubbles in contact with the electrode affect the true current density and act on the cell voltage, particularly through the ohmic resistance and the anodic over-

potential. It is generally understood that hampered gas release from electrodes facing downwards, results in the formation of large bubbles through coalescence [16–18]. Immediately behind these macrobubbles, the anode surface is free of bubbles and fully active. Very soon it becomes covered by small bubbles, growing at active nucleation sites at the anode surface, until they are engulfed by the subsequent macrobubble. Therefore, it has been shown to be appropriate to distinguish between macrobubbles covering an area A^* and forming a fractional bubble coverage [10]

$$\Theta^* \equiv \frac{A^*}{A} \tag{5}$$

and a corresponding bubble coverage pertinent to small bubbles,

$$\Theta^{**} \equiv \frac{A^{**}}{A(1-\Theta^*)} \tag{6}$$

The total fractional bubble coverage is, hence,

$$\Theta \equiv \frac{A^* + A^{**}}{A} = 1 - (1-\Theta^*)(1-\Theta^{**}) \tag{7}$$

4. Components of the cell voltage

Some of the components forming the cell voltage are independent of the alumina concentration. The cathodic overpotential is about $\eta_c \approx 0.05$ V [19], and the ohmic drop in the electrodes may be set approximately at 0.35 V in the cathode and at 0.25 V in the anode for an industrial cell with prebaked anodes and a nominal current density of I/A=7500 A m^{-2} (including the intercell bus bars). All other fractions of the cell voltage depend on the alumina concentration and vary more or less during operation, particularly near the onset of the anode effect.

4.1. *Reversible potential*

The equilibrium potential of the reaction

$$Al_2O_3 + \frac{3}{2}C \rightarrow 2Al + \frac{3}{2}CO_2$$

is calculated from

$$E = \left| E_0 - \frac{RT}{6F} \ln \frac{a_{Al}^2 a_{CO_2}^{3/2}}{a_{Al_2O_3} a_C^{3/2}} \right| \tag{8}$$

where $E_0 = -1.186$ V at 970 °C. Al, CO_2 and C are in their standard states (i.e. $a = 1$). The activity of Al_2O_3 can be calculated from

$$a_{Al_2O_3} = 21.8 w^{1.5} - 1.1 w \tag{9}$$

Equation 9 correlates data by Dewing and Thonstad [20] and is applicable up to alumina saturation.

4.2. *Charge transfer overpotential*

The anodic charge transfer overpotential under consideration of diffusion of reactant A according to the concentration-corrected Butler–Volmer equation for $j \gg j_0$ is

$$\eta_A = \frac{RT}{\alpha F} \ln \frac{(j/j_0)}{(1 - \frac{j}{j_{lim}})} \tag{10}$$

It is advisable to divide the anode area into two regions taking into account that the initially plane underside of the anode is rounded off. Calculations by Zoric et al. [21] have shown that it assumes a definite form after only a few days of operation, whereas the central area remains essentially plane. Gas release in the side area is facilitated, and any effect of gas may be considered negligible there. On the central area, large bubbles formed by coalescence control the current distribution and ohmic voltage drop. If the fraction of the initial area lost by rounding off is f_A and if the fraction of the total current passing through the marginal area $f_A A$ and the anode side walls is f_I, then the actual current density of the central area is

$$j = \frac{I(1-f_I)}{A(1-f_A)(1-\Theta)} = \frac{I}{A} \frac{(1-f_I)}{(1-f_A)(1-\Theta^*)(1-\Theta^{**})} \tag{11}$$

Zoric et al. [21] found that the value f_A depends on the gap to neighbouring anodes and to frozen ledge. The fraction f_I in smooth operation is about 8 to 20% [21]. From mass transfer of reactant A,

$$\frac{I(1-f_I)}{(n/\upsilon_A)F} = k_A A (1-f_A)(1-\Theta^*)(c_{A\infty} - c_{Aw}) \tag{12}$$

follows the limiting current density for $c_{Aw} \rightarrow 0$.

$$j_{lim} \equiv \frac{I_{lim}(1-f_I)}{A(1-f_A)(1-\Theta^*)(1-\Theta^{**})} = \frac{(n/\upsilon_A) F k_A c_{A\infty}}{1-\Theta^{**}} \tag{13}$$

From various experimental investigations [19], a Tafel line

$$\frac{\eta_A}{V} = 0.5 + 0.25 \lg \frac{j}{\mathrm{A/cm^2}} = 0.108 \ln \frac{j}{j_0} \tag{14}$$

may be derived, corresponding to an exchange current density $j_0 = 100$ A m^{-2}. The charge transfer overpotential, Equation 10, results in

$$\eta_A = 0.108\,\mathrm{V} \ln \frac{I/\mathrm{A}}{j_0(1-\Theta^{**})\left[\frac{(1-\Theta^*)(1-f_A)}{1-f_I} - \frac{(I/A)M_A}{(n/\upsilon_A)Fk_A w \rho_L}\right]} \tag{15}$$

The macrobubble coverage Θ^* has been shown [8] to be controlled by wettability and fluid dynamics, whereas

the coverage due to small bubbles, Θ^{**}, is strongly dependent on the actual current density, that is, the current density on the area not covered (or shielded) by large bubbles. The action of the alumina bulk concentration is then twofold: It affects wettability and, in combined action with fluid dynamics, it affects the bubble coverage and thus the actual current density, and it directly controls the limiting current density.

4.2.1. *Mass transfer coefficient*
In industrial cells, where the anode effect has been shown to occur at large values of the bubble coverage Θ^* [9], the resulting current density on the active area $A(1-\Theta^*)$ (not covered by macrobubbles) is large enough to render microconvection induced by small bubbles the controlling mass transfer mechanism [9]. The mass transfer coefficient may be estimated from [22, 23]

$$k_A = C_1 \left[\frac{I(1-f_I)\varepsilon_B f_G}{A(1-f_A)(1-\Theta^*)} \Theta^{**0.5}(1-\Theta^{**})^{0.5} \right]^{0.5} \tag{16}$$

with the abbreviation

$$C_1 \equiv 1.89 \left[\frac{D_A RT}{(n/v)_B Fpd} \right]^{0.5} Sc^{-0.013} \tag{17}$$

where f_G denotes the gas evolution efficiency, i.e. the fraction of the total amount of electrochemically generated substance (CO_2 + CO) evolved as gas in the form of bubbles grown at the electrode surface [24]. At large values of the current density, more strictly at values $\Theta \to 1$, the gas evolution efficiency f_G approaches unity [25]. Evaluation of experimental data [26] and recent theoretical investigations [27] have shown that $f_G \approx 1$ is a reasonable value for all values of $\Theta > 0.2$, which applies to aluminium electrolysis.

4.2.2. *Fractional coverage due to small bubbles*
The fractional coverage due to small bubbles depends on the current density and may be expressed in modification of a previous relationship [26] by

$$\Theta^{**} = \left[\frac{I/A}{(I/A)_{max}} \right]^{0.3} \tag{18}$$

with $(I/A)_{max} \approx 300$ kA m^{-2} derived from experimental data [28]. The empirical equation (18) applies to electrodes facing upwards with stagnant aqueous electrolytes. Flowing electrolytes lower the bubble coverage substantially [29–31]. This effect will here tentatively be taken into account by a factor 0.5. Adaptation to anodes in alumina reduction cells gives

$$\Theta^{**} = 0.5 \left[\frac{I/A}{(I/A)_{max}} \varepsilon_B \frac{1-f_I}{(1-f_A)(1-\Theta^*)} \right]^{0.3} \tag{19}$$

The numerical evaluation below will show that the effect of the uncertain factor on the result is small, and the induced inaccuracy is irrelevant.

4.2.3. *Fractional coverage due to large bubbles*
From a mass balance of gas evolved at the anode surface facing downwards and gas released to the edge of anode, it follows that [8]

$$\frac{I}{A} \frac{\varepsilon_B(1-f_I)RT}{(1-f_A)(n/v_B)Fpv} \frac{A}{HL} = \frac{\Theta^*}{f_G} \tag{20}$$

The bubble velocity depends on the bubble height H, and it may simply be taken into account by a linear relationship [9],

$$\frac{v}{v_{max}} = \frac{H}{H_{max}} \tag{21}$$

The bubble height of large gas bubbles varies with the contact angle ϑ, which depends on the alumina concentration and may be estimated from [8]

$$H = b\sqrt{1+\cos\vartheta} = b\left(1+\cos\frac{2.22}{10^{kw}}\right)^{0.5} \tag{22}$$

with the Laplace parameter

$$b \equiv \sqrt{\frac{2\gamma}{(\rho_L - \rho_G)g}} \tag{23}$$

where $K \approx 2$ is at present a tentative value derived from diverging experimental results [9]. A maximum velocity v_{max} may be attributed to the maximum bubble height at $\vartheta = 0$. With $f_G \approx 1$, Equation 20 takes the form

$$\Theta^* = K_2 \frac{1-f_I}{1+\cos\frac{2.22}{100^w}} \tag{24}$$

with the abbreviation

$$K_2 = \frac{I}{A} \frac{\sqrt{2}\varepsilon_B RTA/L}{(1-f_A)(n/v_B)FpK_3 b v_{max}} \tag{25}$$

4.3. *Diffusion overpotential of dissolved gas*

Since the melt adjacent to the anode is supersaturated with dissolved gas, the activity of the product CO_2 (subscript B) deviates from the standard state. Such supersaturation may attain large values at gas-evolving electrodes [32, 33]. The diffusion overpotential is

$$\eta_B = \frac{RT}{(n/v_B)F} \ln\left(\frac{c_{Bw}}{c_{B\infty}}\right)^{v_B} \tag{26}$$

The concentration ratio follows from mass transfer of dissolved gas from electrode to liquid bulk on the active area,

$$\frac{dN_B}{dt} = \frac{I(1-f_I)\varepsilon_B}{(n/v_B)F} \equiv K_B A(1-f_A)(1-\Theta^*)(c_{Bw} - c_{B\infty}) \tag{27}$$

to result in

$$\eta_B = \frac{RT}{(n/v_B)F} \ln\left[1 + \frac{I\varepsilon_B(1-f_I)}{A(1-f_A)(1-\Theta^*)(n/v_B)FK_B c_{B\infty}}\right] \tag{28}$$

where $c_{B\infty}$ denotes the concentration of dissolved gas in bulk of the melt, being approximately equal to the saturation concentration [34].

4.4. *Ohmic interelectrode resistance*

On the central area, the ohmic interelectrode resistance between the anode surface facing downwards and the cathode is controlled by macrobubbles and by small bubbles in contact with the electrode. Large bubbles cause a nonuniform current distribution at the cathode depending on the bubble radius R. The varying length of the current path in the melt may be taken into account by a simple model from which the ohmic interelectrode voltage drop in the horizontal gap results in

$$U_\Omega = \frac{I}{A}\frac{(1-f_I)Y}{(1-f_A)\kappa}\left[1 + \Theta^*\left(\frac{H}{Y(1-\Theta^*)} + 0.14\frac{R}{Y-H}\right) + \frac{H^{**}}{Y(1-\Theta^*)}\left(\frac{1}{1-\Theta^{**}} - 1\right)\right] \tag{29}$$

where H^{**} denotes the height of small bubbles. An estimate shows that the effect of small bubbles on the ohmic resistance is negligibly small, because $H^{**} \ll Y$ and the particular bubble coverage of small bubbles Θ^{**} is much smaller than unity at the incipience of the anode effect. The total bubble coverage Θ and its components Θ^* and Θ^{**}, shown in Figure 2, ensure the simplification. The ohmic potential drop results in

$$U_\Omega = \frac{I}{A}\frac{(1-f_I)Y}{(1-f_A)\kappa}\left[1 + \Theta^*\left(\frac{H}{Y}\frac{1}{1-\Theta^*} + 0.14\frac{R}{Y-H}\right)\right] \tag{30}$$

where H is given by Equation 20. The conductivity of the melt, κ, depends on the content of alumina, w, on that of other components, and on temperature [35],

$$\kappa = 100\exp\left(1.977 - 2w - 1.31w_{AlF_3} - 0.6w_{CaF_2} - 1.06w_{MgF_2} - 0.19w_{KF} + 1.21w_{LiF} - \frac{1204K}{T}\right)\frac{1}{\Omega\,m} \tag{31}$$

and may be approximated for 960 °C and industrial melt composition for values $w < 0.06$ by

$$\kappa = (224 - 400w)\frac{1}{\Omega\,m} \tag{32}$$

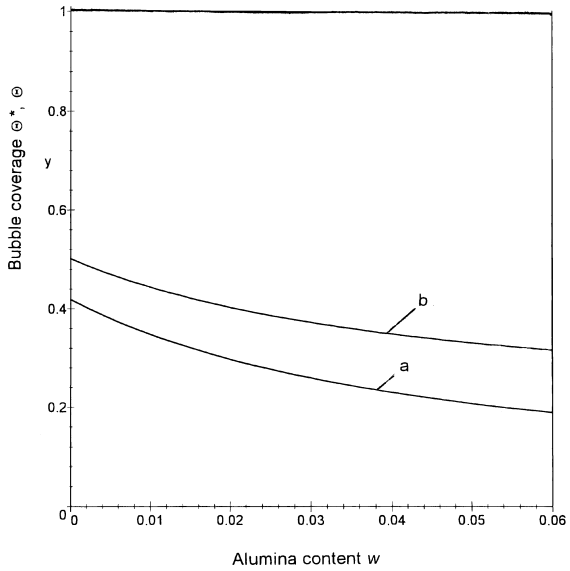

Fig. 2. Fractional bubble coverages of macrobubbles (a) and total bubble coverage (b).

At the anode side area with large inclination, bubbles move with much higher velocity, and their action on current distribution is approximately negligible. Supposing that an ohmic resistance of the current $f_I I$ passing through the side walls is not substantially affected by the alteration in current and set constant, we obtain

$$U_\Omega = \frac{If_I Y}{Af_A\kappa} \tag{33}$$

Combination of Equations 30 and 33 with elimination of the current fraction f_I, gives the interelectrode voltage drop,

$$U_\Omega = \frac{IY}{A\kappa}\left[f_A + \frac{1-f_A}{1 + \Theta^*\left(\frac{H/Y}{1-\Theta^*} + 0.14\frac{R}{Y-H}\right)}\right]^{-1} \tag{34}$$

The fraction of the total current passing through the side walls of the anode, f_I, is essentially affected by the ohmic resistance due to large bubbles, and it thus varies with the fractional gas coverage Θ^*. Comparison with Equation 33 gives

$$f_I = \left[1 + \frac{\frac{1}{f_A} - 1}{1 + \Theta^*\left(\frac{H}{Y(1-\Theta^*)} + 0.14\frac{R}{Y-H}\right)}\right]^{-1} \tag{35}$$

5. Results

The above equations were applied to a typical industrial cell with prebaked anodes, Table 1. We consider an initial underside area of 1 m^2, operating at a nominal current density $I/A = 7500$ A m^{-2} and a temperature of

Table 1. Typical data of an industrial sidebreak cell with prebaked anodes

I/A	7500 A m^{-2}
A	1.0 m^2
A/L	0.24 m
n/v_A	6
n/v_B	3.5
ε_A	0.95
ε_B	1
v_{max}	0.3 m s^{-1}
d	40×10^{-6} m
T	960 °C
p	103000 Pa
ρ_L	2050 kg m^{-3}
γ	0.14 kg s^{-2}
D_A	1.5×10^{-9} m^2 s^{-1}
D_B	1×10^{-9} m^2 s^{-1}
M_A	0.102 kg mol^{-1}
η_L	2.7×10^{-3} kg m^{-1} s^{-1}
K_1	2
f_A	0.15

960 °C. The fraction f_A of the initially plane anode area rounded off by anode wear during operation, may be set to $f_A = 0.15$ [21].

The factor K_2, Equation 25, depends strongly on operational data, some of which are not ascertained. Introduction of typical industrial data [9] with reasonable values of the ratio A/L and the melt velocity v_{max} as estimated from model observations [9], gives $K_2 \approx 0.6$. Further, the mass transfer coefficient from Equation 16 results in $k_A = 0.00027$ to 0.0003 m s^{-1}. To adapt the present model results to data of industrial cells, both values were slightly modified: $K_2 = 0.2$ and $k_A = 0.0001$ m s^{-1} were used. The bubble coverage Θ^{**} of small bubbles was derived from Equations 19 and 35.

Increasing bubble coverage with decreasing alumina fraction w raises the ohmic resistance. The fraction $1 - f_I$ of the total current passing through the horizontal central anode area follows from Equation 35 with an interpolar distance $Y = 0.045$ m, a height H of macrobubbles from Equation 22 with a radius $R = 0.1$ m, is shown in Figure 3. The value of the radius results from observations of bubble volumes of about 100 ml made by Zoric and Solheim [18] on an industrial cell with prebaked anodes.

The anodic charge transfer overpotential was calculated from Equation 15, where the mass transfer coefficient from Equation 16 was calculated with $C_1 = 5.79 \times 10^{-6}$ m^2 $(sA)^{-0.5}$, $f_G = 1$ and $\varepsilon_A = 0.95$, taking account of the fact that alumina is formed by reoxidation in the interelectrode gap.

An estimate of the overpotential component η_B due to dissolved gas is more problematic. The solubility of CO_2 in cryolite melt is about $c_{B\infty} \approx 1$ mol m^{-3} [36, 37], but the solubility of CO is unknown hitherto and may be much lower (as is the case with O_2 [37]). The diffusion coefficient of dissolved CO_2 in cryolite melts, $D_B \approx 10^{-9}$ m^2 s^{-1} [36], is of the same order as that of alumina, permitting at least a rough estimate of the mass transfer coefficient $k_B \approx k_A$. Fortunately, η_B results in small values, and uncertainties will not substantially affect an estimate of the overall cell voltage.

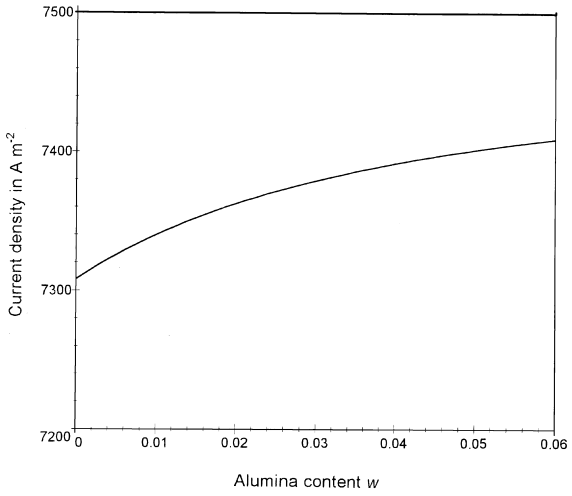

Fig. 3. Average current density of the central anode area against the alumina content. Nominal current density $I/A = 7500$ A m^{-2}.

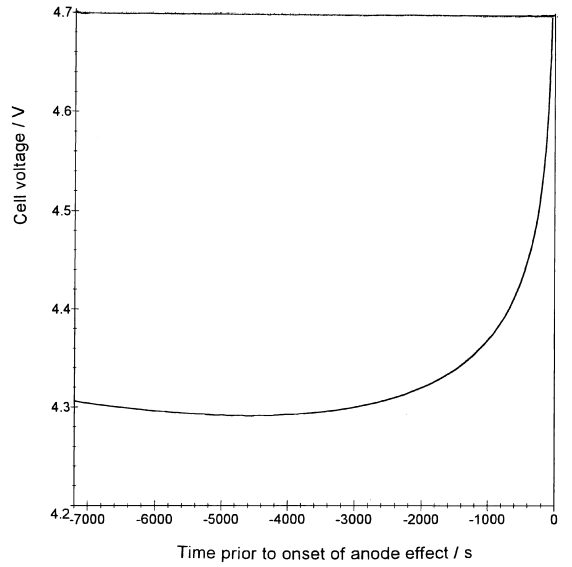

Fig. 4. Long-term increase in cell voltage prior to the onset of anode effect, present model.

The dependence of the cell voltage on time if no fresh alumina is added until the anode effect occurs, results from combination of Equations 4, 24 and 35 with $\rho_L = 2050$ kg m^{-3} and $M_A = 0.102$ Kg mol^{-1}, as shown in Figure 4.

6. Discussion

The cell voltage and its components are shown in Figure 5. It is seen that the cell voltage, as well as the ohmic potential drop in the melt, exhibit minima, whereas the anodic overpotential increases steadily as

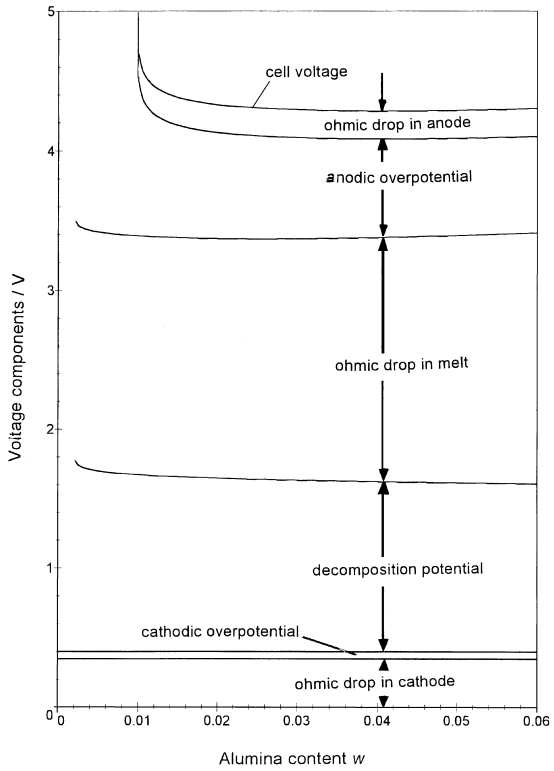

Fig. 5. Components of cell voltage calculated from the model equations.

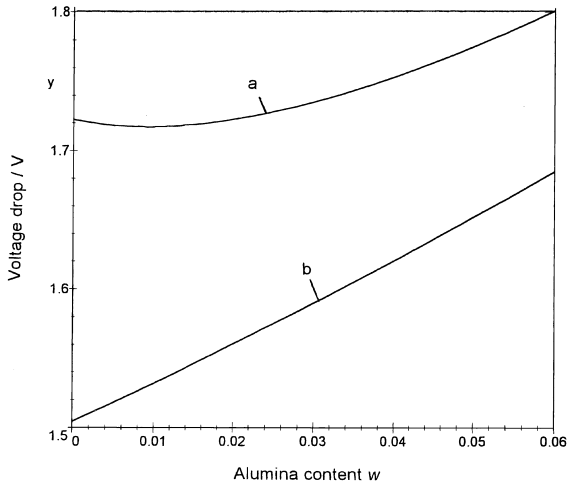

Fig. 6. Ohmic interelectrode voltage drop: (a) calculated from Equation 34, (b) in absence of bubbles.

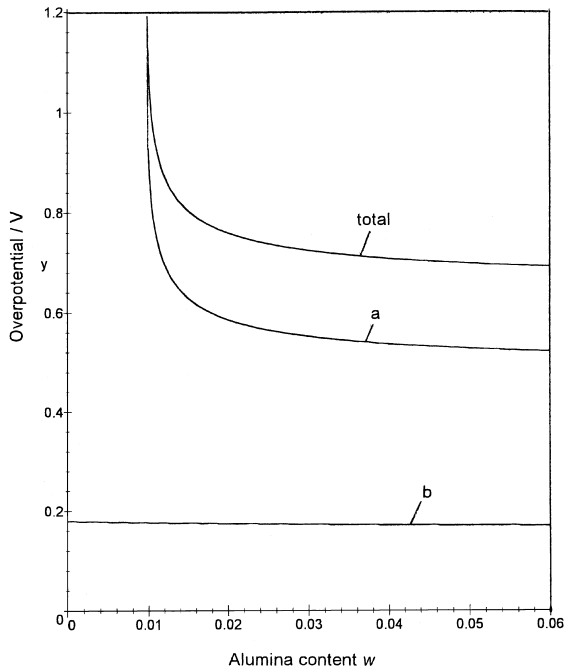

Fig. 7. Anodic charge transfer overpotential (a) and concentration overpotential (b) prior to the onset of the anode effect, calculated from Equations 15 and 28.

the alumina content w decreases. The lines are the result of several interactive effects.

Due to the increase in the bubble coverage values with decreasing alumina content, Figure 2, the nominal current density of the central anode area, $I/A(1-f_I)/(1-f_A)$, decreases, as seen from Figure 3. However, the increasing bubble coverage results in a strong increase in the actual current density, Equation 12, until the limiting current density, Equation 13, is attained, and the anode effect occurs.

The largest voltage component is the ohmic drop in the melt, U_Ω. Its minimum, Figure 6, is the result of two antagonistic effects: (i) the increase in electrical conductivity with decreasing alumina content, according to Equation 32, is predominant at large w values; and (ii) the increasing bubble coverage, mainly of Θ^*, as seen from Equation 35, becomes the controlling parameter at small alumina contents, because the actual current density increases, although the current through the anode underside is decreased.

Figure 6 shows also the ohmic potential drop calculated from Equation 34 for a bubble-free electrolyte. The result is in agreement with the finding by Haupin [38], showing an increase of 0.15 to 0.4 V due to bubbles. An equation to estimate the incremental ohmic drop due to bubbles proposed by Zoric and Solheim [18], gives values that are far higher.

Particular attention is due to the anodic concentration overpotentials referring to alumina, η_A, and to the dissolved gaseous product, η_B, see Figure 7. The component η_B increases steadily and moderately as the alumina content decreases, because the bubble coverage increases and, hence, the actual current density. The corresponding increase in the component η_A is initially equally moderate, but becomes faster as the actual current density approaches the limiting current density, finally leading to an extremely strong increase. The corresponding critical alumina content depends strongly on the mass transfer coefficient k_A, calculated from Equation 16, that is seen to be greatly affected by the bubble coverage.

The variation in cell voltage with the alumina content is mainly affected by the reaction potential, the anodic overpotential and the ohmic potential drop in the melt.

During the very last period prior to the onset of the anode effect, the increase in the anodic overpotential due to alumina becomes predominant, exceeding the other voltage components and finally provoking the onset of the anode effect. The overpotential component due to dissolved gas, η_B, remains small and does not contribute substantially to the anode effect. Both the voltage increase due to the ohmic potential drop and to the anodic overpotential are induced by the macrobubble coverage Θ^*. It is the dominating quantity in controlling the critical alumina content w_c, and it may attain large values [9]. On the other hand, the bubble coverage due to small bubbles, Θ^{**}, (which is uncertain due to the hitherto unknown effect of the flow velocity) varies only slightly and is of little influence, even on the mass transfer coefficient k.

The cell voltage during the very last 10 s prior to the onset of anode effect, calculated from Equation 4 with $K_1 = 2$, is shown in Figure 8, demonstrating a drastic increase, which, according to the present model, is caused by approaching the limiting current density.

The calculated cell voltage during the time after the alumina feeding was stopped until the onset of the anode effect, is shown as the broken line in Figure 1, together with the above-mentioned published data [3–5] and new recordings obtained in industrial sidebreak cells. The agreement is satisfactory, except for the last 100 ms immediately prior to the incipience of the anode effect. This discrepancy may reflect a major change in the electrolysis conditions, possibly due to codischarge of fluoride ions as a result of the depletion of oxygen-containing ions [39]. It leads to the formation of perfluorocarbon gases, which are known to be formed at the onset of the anode effect [40], and which are definitely associated with an increase in cell voltage [41]. As long as the alumina concentration at the interface remains sufficiently high – low values being sufficient – the formation of perfluorocarbons does not occur [42]. As the alumina concentration approaches zero, codeposition of fluorine compounds starts [43], and these are known to reduce the wettability of the surface [16, 44].

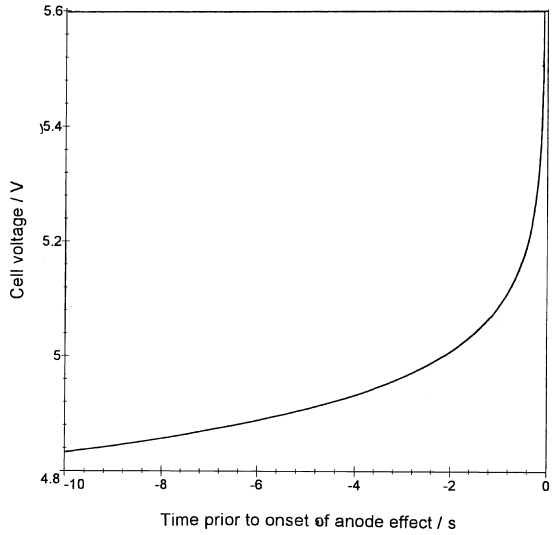

Fig. 8. Increase in cell voltage during the last 10 s prior to the onset of anode effect, present model.

Another reason for the discrepancy may be a faulty assessment of the real point of time for the incipience of the anode effect: A lag of only a few milliseconds results in a substantial deviation from the theoretical line in Figure 1.

In industrial cells, a critical alumina content results from Equation 12:

$$w_c = \frac{I(1-f_I)}{A(1-f_A)(1-\Theta^*)} \frac{M_A}{(n/v_A)Fk_A\rho_L} \tag{36}$$

A precise prediction of the critical value is not possible at present owing to several approximations in the model. Above all, the assumption of perfect mixing in the interelectrode space is questionable. Equation 4 disregards the melt outside the interelectrode space and is restricted to the central anode area where the anode effect is initiated. Furthermore, the true size of the gas bubbles and the resulting bubble coverage are uncertain.

Nonetheless, Equation 36 provides valuable information. It is seen that the value w_c is controlled by the nominal current density I/A, the form of the rounded-off side walls expressed by f_A, the fraction of current, f_I, passing through the central area, the fractional bubble coverage due to macrobubbles, Θ^*, and the mass transfer coefficient k_A, f_I and Θ^* are interrelated according to Equation 35. Equation 16 shows that K_A depends on f_I and on both bubble coverages, Θ^* and Θ^{**}, but the effect of the latter is negligible in the range $0.15 < \Theta^{**} < 0.4$ [22]. Since Θ^* depends on I/A and on f_I, (Equations 24 and 25), the critical alumina content w_c at constant nominal current density I/A is essentially a function only of the bubble coverage due to macrobubbles, Θ^*. As further seen from Equation 24, Θ^* depends on the contact angle and on the parameter K_2 which takes account of the anode geometry, pressure and temperature, and flow velocity. This confirms the finding [9, 10] that the incipience of the anode effect is the result of the combined action of fluid dynamics and wettability of the anode surface. Their variation explains why the critical content w_c in industrial cells varies over a wide range ($0.005 < w_c < 0.025$). The finding supports conclusions on the mechanism of the anode effect to be discussed separately [45].

Acknowledgement

One of the authors (H.V.) greatly appreciates the kind permission of conducting anode effect measurements given by Hydro Aluminium Sunndal, Norway; particularly the assistance of Ola Jakobsen and his staff. Financial support by the German Government, Bundesministerium für Bildung und Forschung, is gratefully acknowledged.

References

1. A.I. Beljaev, M.B. Rapoport and L.A. Firsanova, Metallurgie des Aluminiums, vol. I. Verlag der Technik, Berlin 1956, p. 121ff.
2. P. Drossbach, T. Hashino, P. Krahl and W. Pfeiffer, *Chemie-Ing.-Technik* **33** (1961) 84.
3. M.P. Taylor, B.J. Welch and J.T. Keniry, *J. Electroanal Chem.* **168** (1984) 179.
4. J. Thonstad, F. Nordmo, A.H. Husøy, K.Ø. Vee and D.C. Austrheim, *in* J.P. McGeer (Ed.), 'Light Metals **1984**' (Warrendale, 1984), p. 825.
5. H.J. Meyer and D.G. Earley, 'Light Metals **1986**' (Warrendale, 1986), p. 365.
6. J. Garbarz-Olivier and C. Guilpin, *J. Electroanal Chem.* **91** (1978) 79.
7. R. Bunsen, (Poggendorff's) *Ann. Physik* **92** (1854) 648.
8. H. Vogt, *J. Appl. Electrochem.* **29** (1999) 137.
9. H. Vogt, *J. Appl. Electrochem.* **29** (1999) 779.
10. H. Vogt, *Aluminium* **74** (2000) 598.
11. H. Vogt, *Metall. Mater. Trans.* **31B** (2000) 1225.
12. G. Oesterheld and H. Brunner, *Z. Elektrochemie* **22** (1916) 38.
13. K. Arndt and H. Probst, *Z. Elektrochemie* **29** (1923) 323.
14. J. Thonstad, *Electrochim. Acta* **12** (1967) 1219.
15. P. Novak, I. Roušar, V. Cezner and V. Mejta, *Collect. Czech. Commun.* **46** (1981) 2788.
16. A.J. Calandra, J.R. Zavatti and J. Thonstad, *Electrochim. Acta* **37** (1992) 711.
17. N.E. Richards, *in* B. Welch (Ed.), 'Light Metals **1998**' (Warrendale, 1998), p. 521.
18. J. Zoric and A. Solheim, *J. Appl. Electrochem.* **30** (2000) 787.
19. K. Grjotheim, C. Krohn, M. Malinovský, K. Matiasovský and J. Thonstad, 'Aluminium Electrolysis' (Aluminium-Verlag, Düsseldorf 1977; 2nd edn 1982).
20. E.W. Dewing and J. Thonstad, *Metall. Mater. Trans.* **28B** (1997) 1089.
21. J. Zoric, I. Roušar and J. Thonstad, *J. Appl. Electrochem.* **27** (1997) 916.
22. K. Stephan and H. Vogt, *Electrochim. Acta* **24** (1979) 11.
23. H. Vogt, *Electrochim. Acta* **29** (1984) 175.
24. H. Vogt, *Surf. Technol.* **17** (1982) 301.
25. H. Vogt, *Electrochim. Acta* **29** (1984) 167.
26. H. Vogt, *J. Electrochem. Soc.* **137** (1990) 1179.
27. H. Vogt, unpublished investigations.
28. R. Piontelli, B. Mazza and P. Pedeferri, A. Tognoni, *Electrochim. Metall.* **2** (1967) 257.
29. C.W.M.P. Sillen, The effect of gas bubble evolution on the energy efficiency in water electrolysis. Dissertation Tech. Hogeschool Eindhoven (1983).
30. R.H.S. Winterton, *Int. J. Heat Mass Transfer* **27** (1984) 1422.
31. J. Eigeldinger and H. Vogt, *Electrochim. Acta* **45** (2000) 4449.
32. S. Shibata, *Denki Kagaku* **44** (1976) 709.
33. H. Vogt, *J. Appl. Electrochem.* **23** (1993) 1323.
34. H. Vogt, *Z. Phys. Chemie* **172** (1991) 123.
35. J. Hives, J. Thonstad, A. Sterten and P. Fellner, *in* U. Mnnweiler (Ed.), 'Light Metals **1994**' (Minerals, Metals & Materials Soc., Warrendale, 1994), p. 187.
36. D. Bratland, K. Grjotheim, C. Krohn and K. Matzfeldt, *J. Metals* **19**(10) (1967) 19.
37. H. Numata and J.O'M. Bockris, *Metallurg. Trans.* **15B** (1984) 39–46.
38. W.E. Haupin, *J. Metals* **23**(10) (1971) 46.
39. G. Flusin, *Z. Elektrochemie* **18** (1912) 174.
40. J. Thonstad, F. Nordmo and K. Vee, *Electrochim. Acta* **18** (1973) 27.
41. A. Øygard, T.A. Halvorsen and J. Thonstad, 'Light Metals **1995**' (Warrendale, 1995), p. 279.
42. W.D. Treadwell and A. Köhl, *Helv. Chim. Acta* **9** (1926) 681.
43. A.J. Calandra, C.E. Castellano, C.M. Ferro and O. Cobo, *in* J.E. Andersen (Ed.), 'Light Metals **1982**' (Warrendale, 1992), p. 345.
44. V. Schischkin, *Z. Elektrochemie* **33** (1927) 83.
45. H. Vogt and J. Thonstad, 'Light Metals **2002**' to be published.